Heterometallic Benzenehexathiolato Coordination Nanosheets: Periodic Structure Improves Crystallinity and Electrical Conductivity

Ryojun Toyoda, Naoya Fukui, Dionisius H. L. Tjhe, Ekaterina Selezneva, Hiroaki Maeda, Cédric Bourgès, Choon Meng Tan, Kenji Takada, Yuanhui Sun, Ian Jacobs, Kazuhide Kamiya, Hiroyasu Masunaga, Takao Mori, Sono Sasaki, Henning Sirringhaus,* and Hiroshi Nishihara*

Coordination nanosheets are an emerging class of 2D, bottom-up materials having fully π-conjugated, planar, graphite-like structures with high electrical conductivities. Since their discovery, great effort has been devoted to expand the variety of coordination nanosheets; however, in most cases, their low crystallinity in thick films hampers practical device applications. In this study, mixtures of nickel and copper ions are employed to fabricate benzenehexathiolato (BHT)-based coordination nanosheet films, and serendipitously, it is found that this heterometallicity preferentially forms a structural phase with improved film crystallinity. Spectroscopic and scattering measurements provide evidence for a bilayer structure with in-plane periodic arrangement of copper and nickel ions with the $NiCu_2BHT$ formula. Compared with homometallic films, heterometallic films exhibit more crystalline microstructures with larger and more oriented grains, achieving higher electrical conductivities reaching metallic behaviors. Low dependency of Seebeck coefficient on the mixing ratio of nickel and copper ions supports that the large variation in the conductivity data is not caused by change in the intrinsic properties of the films. The findings open new pathways to improve crystallinity and to tune functional properties of 2D coordination nanosheets.

1. Introduction

Coordination nanosheets are a new class of 2D materials constructed from hybridization of transition metal centers and organic bridging ligands.[1] A broad range of planar structures is accessible by combining these building blocks. Coordination nanosheets have been investigated for applications in electrocatalysis,[2] energy storage,[3] electronic devices,[4] and others.[5] The original discovery of a nickelladithiolene nanosheet ($Ni_{1.5}BHT$) reported in 2013 used benzenehexathiolato (BHT) as the ligand.[6] BHT is one of the simplest ligands, having six thiolato groups attached to a benzene ring. The square-planar coordination sphere of the nickel center provides a fully π-conjugated plane; thus, the resulting films exhibit high electrical conductivities (1.6×10^2 S cm^{-1} at 300 K).[7] Since their first discovery, various coordination nanosheets based

R. Toyoda, N. Fukui, H. Maeda, C. M. Tan, H. Nishihara
Department of Chemistry, Graduate School of Science
The University of Tokyo
7-3-1 Hongo, Bunkyo-ku, Tokyo 113-0033, Japan
E-mail: nisihara@rs.tus.ac.jp
N. Fukui, E. Selezneva, H. Maeda, C. M. Tan, K. Takada, H. Nishihara
Research Center for Science and Technology
Tokyo University of Science
2641 Yamazaki, Noda, Chiba 278-8510, Japan
D. H. L. Tjhe, E. Selezneva, Y. Sun, I. Jacobs, H. Sirringhaus
Cavendish Laboratory
University of Cambridge
JJ Thomson Avenue, Cambridge CB3 0HE, UK
E-mail: hs220@cam.ac.uk

E. Selezneva, C. Bourgès, T. Mori
WPI International Center for Materials Nanoarchitechtonics (WPI-MANA)
National Institute for Materials Science (NIMS)
Namiki 1-1, Tsukuba 305-0044, Japan
K. Kamiya
Research Center for Solar Energy Chemistry
Osaka University
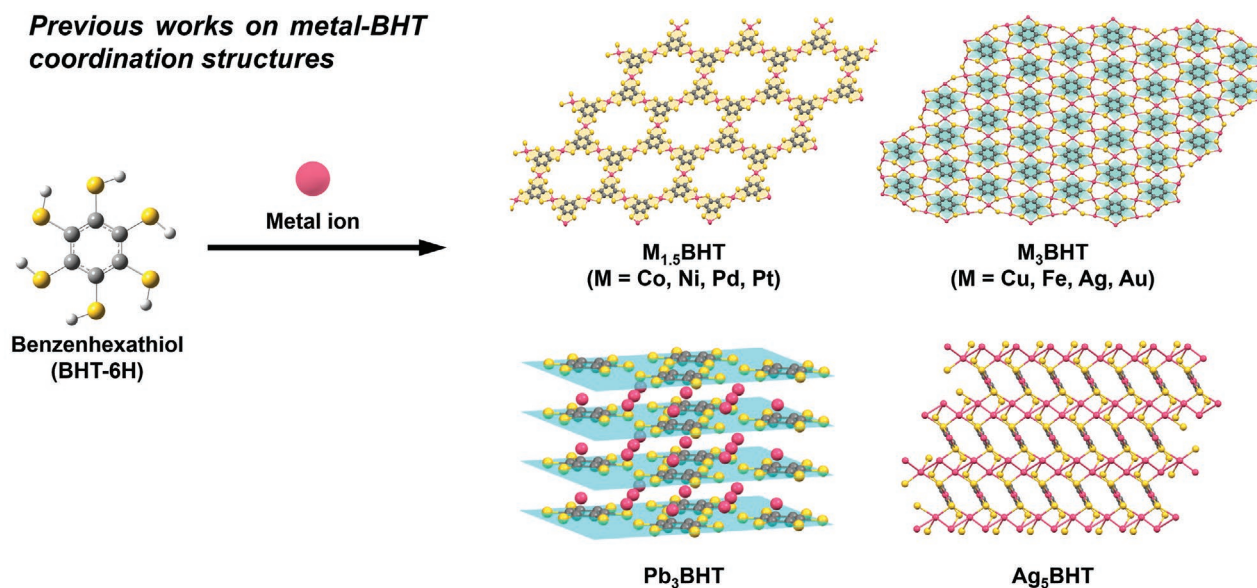1–3 Machikaneyama, Toyonaka, Osaka 560-8531, Japan
K. Kamiya
Graduate School of Engineering Science
Osaka University
1–3 Machikaneyama, Toyonaka, Osaka 560-8531, Japan
H. Masunaga
Japan Synchrotron Radiation Research Institute (JASRI)
1-1-1 Kouto, Sayo-cho, Sayo-gun, Hyogo 679-5198, Japan
S. Sasaki
Faculty of Fiber Science and Engineering
Kyoto Institute of Technology
1 Matsugasaki Hashikami-cho, Sakyo-ku, Kyoto 606-8585, Japan
S. Sasaki
RIKEN SPring-8 Centre
1-1-1 Kouto, Sayo-cho, Sayo-gun, Hyogo 679-5148, Japan

The ORCID identification number(s) for the author(s) of this article can be found under https://doi.org/10.1002/adma.202106204.

a *Previous works on metal-BHT coordination structures*

Benzenehexathiol (BHT-6H)

Metal ion

$M_{1.5}BHT$
(M = Co, Ni, Pd, Pt)

M_3BHT
(M = Cu, Fe, Ag, Au)

Pb_3BHT

Ag_5BHT

b *This work on heterometal-BHT coordination nanosheets*

Liquid/liquid interfacial synthesis

Mixed metal ions

BHT-6H

Aqueous phase

Organic phase

At the interface

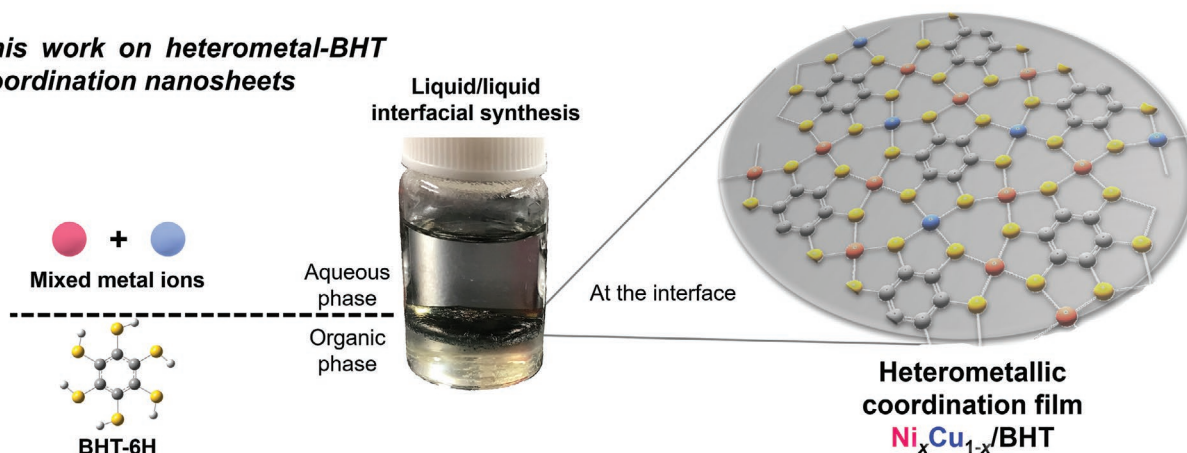**Heterometallic coordination film Ni_xCu_{1-x}/BHT**

Figure 1. a) Previous examples of coordination structures constructed from benzenehexathiolato ligands. b) Preparation of heterometallic coordination nanosheets Ni_xCu_{1-x}/BHT using liquid/liquid interfacial synthesis.

on BHT have been reported. It is interesting that despite the simplicity of BHT, the resulting compounds exhibit diverse structures, depending on the metal centers (**Figure 1**a). When cobalt,[8] palladium,[9] or platinum[10] are employed, a kagome-lattice structure similar to that of nickel is proposed ($M_{1.5}BHT$), while copper,[11] silver,[12] gold,[12] and iron[13] form more densely packed planar structures (M_3BHT). In addition, lead and silver ions produce unique 3D networks.[14] This structural dependence on metal centers is one of the attractive features of coordination polymers and motivated us to examine the effect of heterometallicity (a combination of different metal ions) on frameworks of BHT-based coordination nanosheets.

One of the most difficult research challenges remains the poor long-range crystalline order that typically results when films of coordination nanosheets are grown by a solution process, for example at a liquid–liquid interface.[6] Films typically comprise small nanocrystalline domains with poor orientational control. The poorly ordered microstructure makes it difficult to study structure-property relationships and limits

device performance. Several approaches have been proposed to improve crystallinity. Most commonly these involve minimizing mechanical perturbations to the liquid–liquid interface or adjusting reaction conditions, such as addition of a base that deprotonates the ligand and an oxidizing agent that oxidizes it.[15] However, this has achieved limited success. A recent promising strategy has been to design the organic ligand to be electron-deficient in order to increase the acidity of the metal-binding group and to make metal-ligand bond formation more reversible.[16] However, this strategy is not straightforward to apply to the small BHT ligand that has yielded the highest electrical conductivities to date.

In this study, exploiting the design flexibility of bottom-up materials, we investigated a new series of coordination nanosheets produced by introduction of two different metal ions. Such heterometallic coordination nanosheets have previously been reported, based on hexaaminotriphenylene; however, no evidence for improved structural order was found and the electrical conductivities observed were comparatively low

(< 55 S cm^{-1}).[17] Nickel and copper ions were employed here, as they have similar ionic radii. Heterometallic films were prepared at a liquid–liquid interface by changing the mixing ratio of the two metal ions in the aqueous phase (Figure 1b). The film produced under the condition of nickel ion mixing ratio x is expressed as Ni$_x$Cu$_{1-x}$/BHT by inserting "/". This simple strategy proved effective to partially replace one metal with the other without phase-separation, and a new structural phase appeared with an intermediate mixing ratio of the metal ions. To our surprise, X-ray diffraction measurements revealed that the new phase possesses higher film crystallinity than pure nickel and copper films. This unexpected phenomenon is reasoned from the interlayer stacking and ordered in-plane metal arrangement of NiCu$_2$BHT that produced larger and better oriented domain microstructures. We investigated the charge transport properties of these heterometallic films with conductivity and Seebeck measurements, the results of which are fully consistent with the structural analysis. In some of our heterometallic films of the new phase, we were able to achieve conductivities up to 1300 S cm^{-1} with a metallic temperature dependency, which are among the highest observed in 2D coordination nanosheets. There is no indication that mixing of metals leads to electronic disorder.

2. Results and Discussion

Similar to previously reported homometallic nanosheets (Ni$_{1.5}$BHT and Cu$_3$BHT), a heterometallic film Ni$_x$Cu$_{1-x}$/BHT

(x: 0.1–0.9) was prepared at a liquid–liquid interface of a dichloromethane solution of BHT and an aqueous solution of metal acetate. The latter included nickel and copper acetate at a ratio of x:(1 − x). Keeping the interface still for 12 h produced a film of µm-order thickness with metallic luster. The detailed experimental procedure is provided in Experimental Methods.

First, the prepared Cu$_3$BHT was characterized by 2D grazing incidence, wide-angle, X-ray scattering (2D GIWAXS). The experimental diffraction peaks were well reproduced by the lattice parameters for Cu$_3$BHT previously reported ($a = 15.016$ Å, $b = 8.691$ Å, $c = 3.489$ Å, $\alpha = \gamma = 90°$, $\beta = 101.50°$).[11b] The film exhibited its 001 diffraction, which reflects the layered structure, with a preferential out-of-plane orientation suggesting a preferential face-on orientation of the layers. However, there is also a more ring-shaped 001 scattering background and the other diffractions are observed with an isotropic pattern (**Figure 2**a) indicating the presence of randomly oriented crystal domains, which is often observed with thick coordination films.[11a] Similarly, 2D GIWAXS analysis was carried out for the nickel homometallic film and ring patterns were observed (Figure 2b). Here, by excluding the counter cation source, we obtained a new structure for the pure nickel nanosheet instead of the previously reported kagome structure of Ni$_{1.5}$BHT.[6,7] The diffraction pattern resembled that of Cu$_3$BHT, and a hexagonal lattice of Ni$_3$BHT with $a = b = 8.38$ Å, $c = 3.48$ Å was derived from the results. Here, we call this structure Ni$_3$BHT. In our previous experiments, sodium bromide (NaBr) was used to provide Na$^+$ ions as counter cations to the anionic nanosheet Ni$_{1.5}$BHT; however, in order to coordinate the experimental
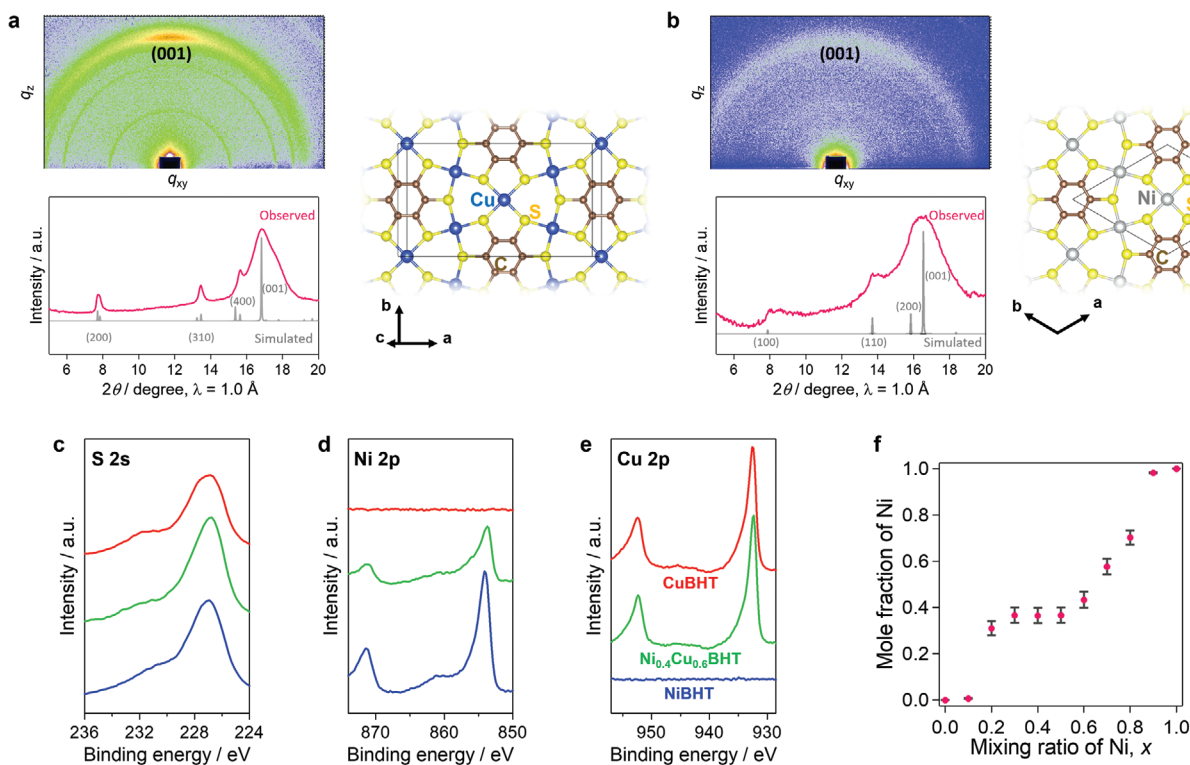

Figure 2. a) 2D GIWAXS pattern, plot and a unit cell structure of Cu$_3$BHT. b) 2D GIWAXS pattern, plot and a unit cell structure of Ni$_3$BHT. c–e) XP spectra for homometallic and heterometallic films, Ni$_x$Cu$_{1-x}$/BHT, focusing on region of c) S 2s, d) Ni 2p, and e) Cu 2p. f) Actual mole fraction of nickel ion in prepared films estimated from relative XPS peak intensities of Ni 2p$_{3/2}$ and Cu 2p$_{3/2}$. Error bars represent systematic errors.

condition with its copper counterpart, NaBr was not added to the aqueous layer in the present study, expecting formation of a charge-neutral state of the nanosheet. It is plausible that the absence of Na^+ ion allowed Ni_6BHT^{6+} subunits to locate inside the pores of the kagome structure, affording the Ni_3BHT framework. Very recently, Dincǎ's group has also reported a similar non-porous structure of Ni_3BHT, which they made from $NiCl_2 \cdot 6H_2O$ without adding counter cations.[18] The structural similarity between Ni_3BHT and Cu_3BHT films enables both nickel and copper ions to be located at the same positions in the plane lattice when a mixed solution of these metal ions is employed.

Figure 2c-e shows the X-ray photoelectron spectra (XPS) of Ni_xCu_{1-x}/BHT for $x = 0$, 0.4, and 1. Ni $2p_{3/2}$ and Cu $2p_{3/2}$ peaks of $Ni_{0.4}Cu_{0.6}/BHT$ can be found at 853.7 and 932.4 eV, respectively. These positions are consistent with those of the corresponding homometallic nanosheets, which suggests that nickel and copper atoms in $Ni_{0.4}Cu_{0.6}/BHT$ are in the same chemical environments as Ni_3BHT and Cu_3BHT, respectively. The peak tops of S 2s spectra of these films are located around 226.9 eV, corresponding to the 0/−1 mixed valence oxidation states reported for $Ni_{1.5}BHT$ nanosheet.[6] Taking into consideration that the XPS peaks of Ni $2p_{3/2}$ and Cu $2p_{3/2}$ are shifted toward low binding energy from the typical +2 state,[11a] the metal ions are at a state between +1 and +2 states as a result of charge transfer from the sulfur atoms toward the metal centers. Figure 2f shows the nickel mole fraction of Ni_xCu_{1-x}/BHT series with respect to the total number of metal atoms, estimated from the ratio of the peak areas of Ni $2p_{3/2}$ and Cu $2p_{3/2}$ in consideration of the detection sensitivity (Figure S1, Supporting Information). The nickel mole fraction of the nanosheet increases with the increased nickel ion ratio in the aqueous layer in preparation. A plateau was found in the x range of 0.3–0.6, which preferentially produced films with a metal ratio of Ni:Cu = 1:2.

X-ray diffraction measurements were performed to clarify the structure of these heterometallic films. Heterometallic films were investigated using 2D GIWAXS. In **Figure 3**a and Figure S2 (Supporting Information), 2D GIWAXS patterns of Ni_xCu_{1-x}/BHT are depicted. The typical thickness of GIWAXS samples was 200–400 nm, which is comparable to those for conductivity measurement (vide infra). As Zhu's group previously reported low crystallinity in a thick Cu_3BHT film (200 nm), the homometallic films showed broad scattering patterns, suggesting the small size and isotropic arrangement of the crystalline domain. However, a part of the heterometallic films such as $Ni_{0.4}Cu_{0.6}/BHT$ (Figure 3b) and $Ni_{0.3}Cu_{0.7}/BHT$ displayed scattering spots rather than rings and showed better crystallinity and anisotropy. It is remarkable that this crystallinity improvement was achieved in relatively thick films (Figure S3, Supporting Information). Judging from the anisotropic scattering patterns, films grow in a specific direction at the liquid–liquid interface when two metal ions are mixed with an appropriate ratio. Looking at the in-plane diffraction peaks of the heterometallic films around 7.8° (Figure 3c), we observe that the lattice for a film with $x = 0.8$ or 0.9 is almost the same as that for Ni_3BHT, suggesting that some nickel ions are replaced with copper ions without changing the lattice structure. The same may be said for the copper-dominant films with $x = 0.1$

and 0.2. Hence, small blending ratios of nickel or copper ion do not alter the lattice structures. When films were prepared with NaBr, a structure similar to $Ni_{1.5}BHT$ was obtained for $Ni_{0.8}Cu_{0.2}/BHT$, where Na^+ ions are thought to be located in the pores of the kagome structure (Figure S4, Supporting Information). Meanwhile, intermediate ratios such as $x = 0.4$ produced sharper peaks both in the in-plane and out-of-plane diffractions. This tendency is consistent with the abundance ratio estimated by XPS.

We also examined film morphology using scanning electron microscopy (SEM, Figure 3e–g; Figure S8, Supporting Information) and atomic force microscopy (AFM, Figure S9, Supporting Information). The Ni_3BHT (Figure 3e) and $Ni_{0.8}Cu_{0.2}/BHT$ (Figure S8a, Supporting Information) films appear more disordered and exhibit very rough surface morphology with RMS surface roughness values on the order of 400 nm (Figure S9a, Supporting Information). In contrast, Cu_3BHT films (Figure 3g) showed much smoother surface morphology with roughness in the range of 10 nm (Figure S9f, Supporting Information) and clearly resolved crystalline domains of tens of nanometers (inset of Figure 3g). These films exhibit some crater-like features (Figure S9e, Supporting Information) that are potentially generated when the solvent is removed from the films. Further optimisation will be needed to eliminate these features. However, importantly, the $Ni_{0.4}Cu_{0.6}/BHT$ and $Ni_{0.6}Cu_{0.4}/BHT$ mixed metal nanosheets show smooth surfaces similar to that of Cu_3BHT, with crystalline domains that are significantly larger (220 ± 60 nm), inset of Figure 3f, compared to 110 ± 10 nm in Cu_3BHT, see Figure 3g). These observations are fully consistent with the X-ray data.

Transmission electron microscopy – energy dispersive X-ray spectroscopy (TEM-EDS) analysis of $Ni_{0.4}Cu_{0.6}/BHT$ was carried out to prove the absence of phase isolation, i.e., a single heterometallic phase is preferentially formed, and the results are displayed in **Figure 4**. In a TEM image, a crystalline fraction of $Ni_{0.4}Cu_{0.6}/BHT$ was found as a hexagonal structure with the distance between bright spots of 8.7 Å, corresponding to neighboring benzene rings of our models, 8.5 Å (Figure 4a,b). This solitary fraction was analyzed by TEM-EDS and the homogeneous distribution of C, S, Ni, and Cu was revealed (Figure 4c). The atomic ratio between Ni and Cu was estimated to be Ni:Cu = 36:64, which is almost the same as 1:2 (Figure 4d). These results well support our claim that $Ni_{0.4}Cu_{0.6}/BHT$ is a stoichiometric compound $NiCu_2BHT$. In addition, a high-angle annular dark-field scanning TEM (HAADF-STEM) image of $Ni_{0.4}Cu_{0.6}/BHT$ (Figure S6a,b, Supporting Information) directly visualized the kagome structure of metal ions.

Further investigation using powder X-ray diffraction, inductively coupled plasma (ICP) analysis, scanning TEM (STEM)-EDS analysis, and Raman spectroscopy confirmed the formation of a single heterometallic phase of $Ni_{0.4}Cu_{0.6}/BHT$ (see Section 2 in Supporting Information).

XPS, X-ray diffraction and TEM-EDS results indicate that a heterometallic phase with a fixed composition ($NiCu_2BHT$) is preferentially formed when nickel and copper ions are mixed. We performed EXAFS measurements of Ni_3BHT, Cu_3BHT, and $Ni_{0.4}Cu_{0.6}/BHT$ in order to obtain further information about their atomic structures. Judging from extended X-ray absorption fine structure (EXAFS) analyses of $Ni_{0.4}Cu_{0.6}/BHT$, its
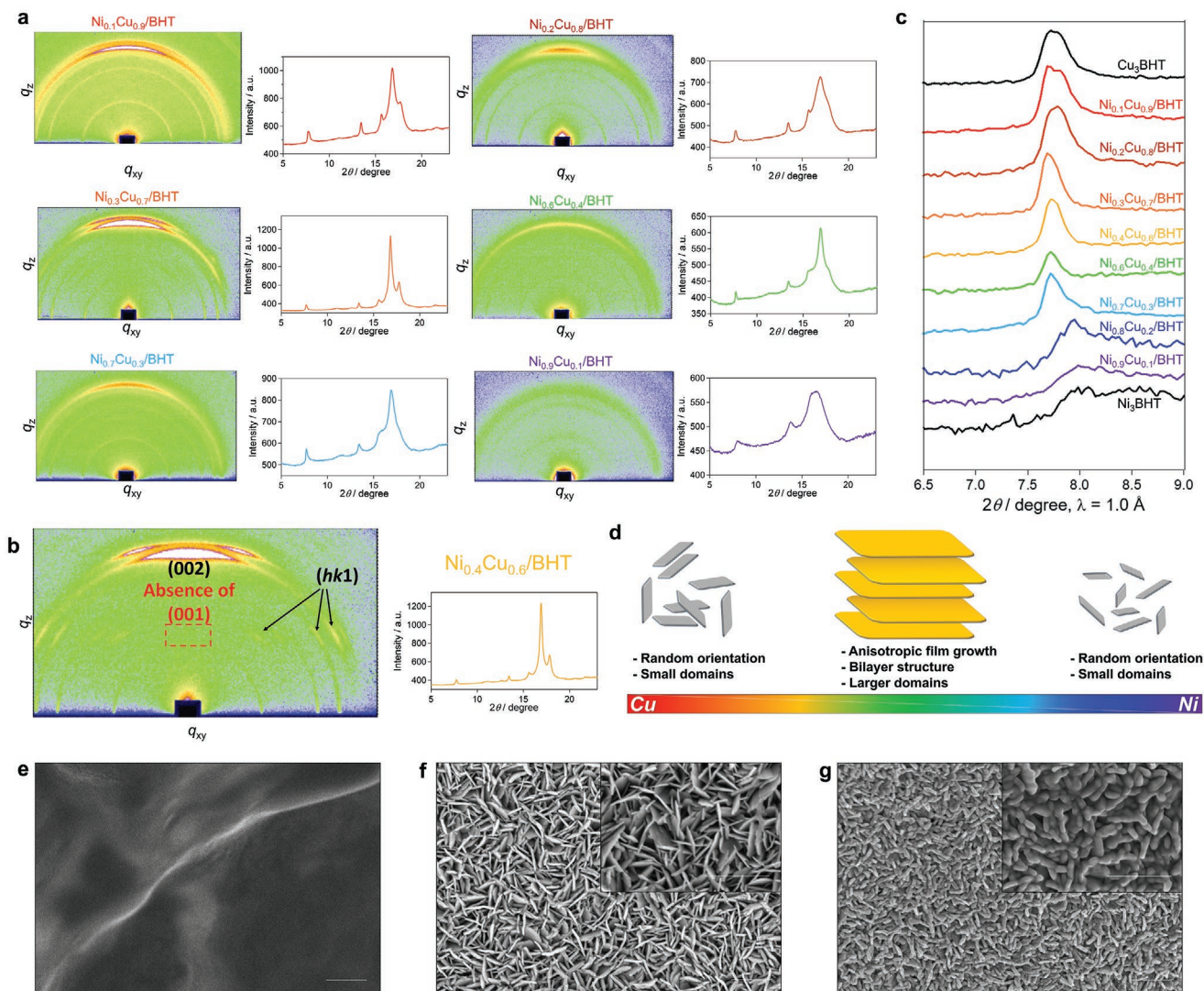
**ADVANCED
SCIENCE NEWS**

www.advancedsciencenews.com

**ADVANCED
MATERIALS**

www.advmat.de

Figure 3. a) 2D GIWAXS patterns and plots of Ni_xCu_{1-x}/BHT films. b) 2D GIWAXS pattern and plot of $Ni_{0.4}Cu_{0.6}$/BHT film. c) In-plane plots from 2D GIWAXS patterns. Numerical values denote Millar indices. For these measurements, X-rays with a wavelength of 1.0 Å were used. d) Illustration of film crystallinity differences between films with different metal ratios. e–g) Secondary electron images of e) Ni_3BHT, f) $Ni_{0.4}Cu_{0.6}$/BHT, and g) Cu_3BHT. Scale markers correspond to 500 nm.

Ni–S distance was 2.21 Å, which is longer than that of Ni_3BHT (2.18 Å), but shorter than the Cu–S distance of Cu_3BHT (Figure S10, Supporting Information). Since $Ni_{0.4}Cu_{0.6}$/BHT has nearly the same lattice constant as Cu_3BHT (details are shown later), the sulfur atoms are more attracted by nickel ions than copper atoms. The EXAFS analyses also suggest that four sulfur atoms coordinate to a nickel atom in $Ni_{0.4}Cu_{0.6}$/BHT (Figure S11, Supporting Information). This supports our model, nickel-substituted Cu_3BHT framework.

Improved crystallinity and anisotropic growth of the film allowed us to distinguish its in-plane and out-of-plane diffraction peaks. Compared with Cu_3BHT, heterometallic $Ni_{0.4}Cu_{0.6}$/ BHT not only has a similar out-of-plane diffraction peak, but also additional peaks in diagonal directions (Figure S12, Supporting Information). As no Cu_3BHT-type unit cell can explain these diffractions, another unit cell was prepared for a bilayer structure. The diagonal peaks and the intense out-of-plane

diffraction could be assigned as ($hk1$) and (002), respectively (Figure 3b). Interestingly, the (001) diffraction is missing in the case of the heterometallic sample. If the two layers have different compositions or different in-plane arrangements, (001) diffraction is expected to appear in the same line with the ($hk1$) peaks. The absence of the (001) means that an extinction rule is working, disclosing that the two layers have the same in-plane structure. Therefore, the possibility of simple stacking of Cu_3BHT and Ni_3BHT layers is excluded. Considering that the structures for the two homometallic nanosheets (Ni_3BHT and Cu_3BHT) are quite similar, it is extraordinary that just an easy blending of the two metal ions resulted in a unique structure, rather than a structure similar to those of the pure materials with metal substitution. This indicates the presence of periodicity in metal arrangement in the 2D structure. With these hints, preparation of a model structure for $NiCu_2BHT$ was attempted.
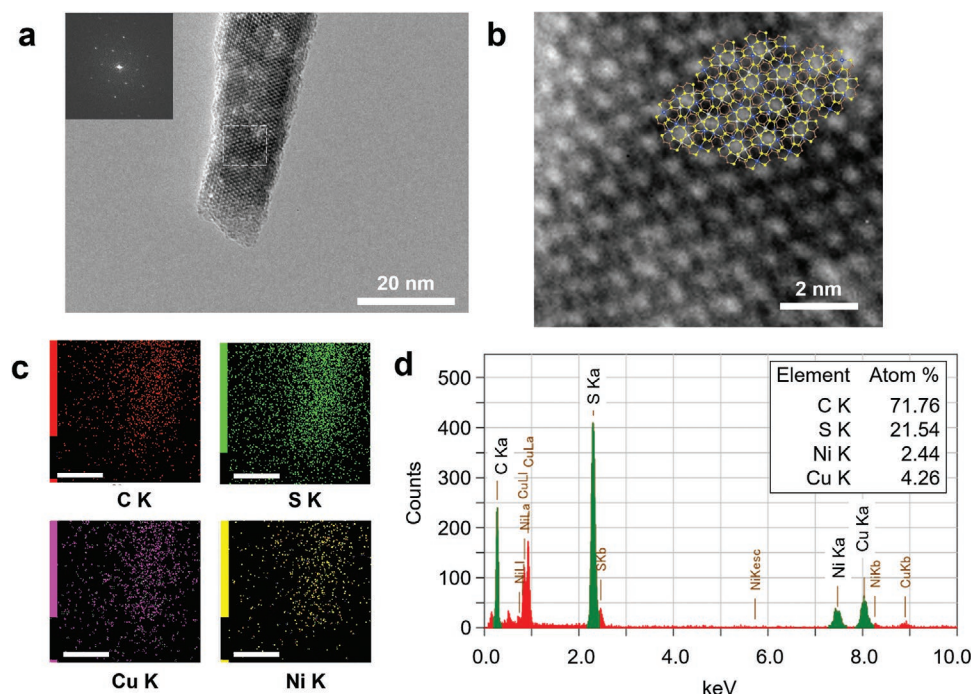
ADVANCED
SCIENCE NEWS

www.advancedsciencenews.com

ADVANCED
MATERIALS

www.advmat.de

Figure 4. a) A TEM image of $Ni_{0.4}Cu_{0.6}$/BHT with its Fourier-transform image. b) A magnified image of the area enclosed by the white dashed line in (a). The structure of model 3 is overlaid. c) Elemental mappings measured by STEM-EDS at the same position as (a). d) The overall EDS spectrum.

First, several bilayer models were constructed by changing the stacking of two layers as shown in **Figure 5**a (models 1, 3, and 5). Also, models with interlayer slips were also prepared (models 2, 3, and 4). Their diffraction patterns were simulated and compared with the experimental result in Figure 5b. Among these models, model 3 or model 4 matches the experimental result best, in particular, model 4 explains the peaks for (hk1). However, we could not assign all the peaks with a single model. Therefore, it is suggested that in the thick films there are several stacking patterns, including stacking distortion, and they are overlapped in the diffraction pattern. In both models 3 and 4, the two layers are positioned to make the interlayer metal-sulfur distance short, which is thought to be responsible for the improvement in film crystallinity.

Next, in order to identify the in-plane arrangement of the two metal ions in the $NiCu_2BHT$ structure, the Cu_3BHT and $Ni_{0.4}Cu_{0.6}$/BHT films were subjected to anomalous grazing incidence wide-angle X-ray scattering (AGIWAXS). By using pre- and post-edge X-ray energies (8980 and 9010 eV) of the Cu K-edge, the contribution of copper ions to the scattering peaks can be highlighted. Here, we normalized peak intensities by the first contribution from the low q and focused on the intensity change in the second peak. In the case of Cu_3BHT, the first two peaks can be assigned to (200) and (310), respectively (Figure 5c). The scattering intensity of (310) with the lower X-ray energy, $I_{CuBHT, 8980 eV}$, was 4.1, while the higher X-ray energy gave the reduced intensity $I_{CuBHT, 9010 eV}$ of 1.4. Meanwhile, only a small change could be seen in the intensity of the second peak as for the $Ni_{0.4}Cu_{0.6}$/BHT film ($I_{Ni0.4Cu0.6, 8980 eV}$ of 1.7, $I_{Ni0.4Cu0.6, 9010 eV}$ of 1.2, Figure 5d). From this result, we deduced a plausible metal arrangement for the $NiCu_2BHT$ structure where Ni ions shape a kagome structure as in $Ni_{1.5}BHT$ and

Cu_6BHT units are incorporated into the pores (Figure 5e). The unit cell for this structure includes $NiCu_2BHT$, and both of the scattering factors of $(2\bar{1}0)$ (the first peak) and (300) (the second peak) can be expressed as $F(2\bar{1}0) = F(300) = -f(Ni) - 2f(Cu)$ (only contributions from the metal ions are considered, as their values are much larger than those of sulfur and carbon atoms, Figure S13, Supporting Information), which supports the unchanged relative intensity of the first two peaks. To validate this structure, we prepared other models for periodic and random arrangements of metal ions as comparisons. Though peak intensities could not be reproduced by a simulation program VESTA (Figure S14, Supporting Information), none of the comparisons gave the same structure factors between the first two peaks, supporting the plausibility of the proposed periodic structure.

The electrical conductivity, σ, was first investigated using the van der Pauw method on the batches of thick ($\approx$1–2 μm) films prepared following the recipe used for all other experiments (reaction time 12 h) (details of the experiment are provided in Experimental Methods). Some of the thick, heterometallic films exhibited very high conductivities (see discussion below), but there were significant batch-to-batch variations. These are likely due to such thick films tending to form surface cracks and other structural defects affecting the reproducibility between the batches (Figure S15, Supporting Information). Another reason for the variations in the electrical conductivity could be the surface roughness that increased as the films were getting thicker (Figures S3 and S9, Supporting Information), which impeded the accurate determination of the film thickness needed for the calculation of conductivity values. These effects were mitigated by preparing thinner films ($\approx$100 nm with surface roughness $\approx$5 nm) by decreasing the
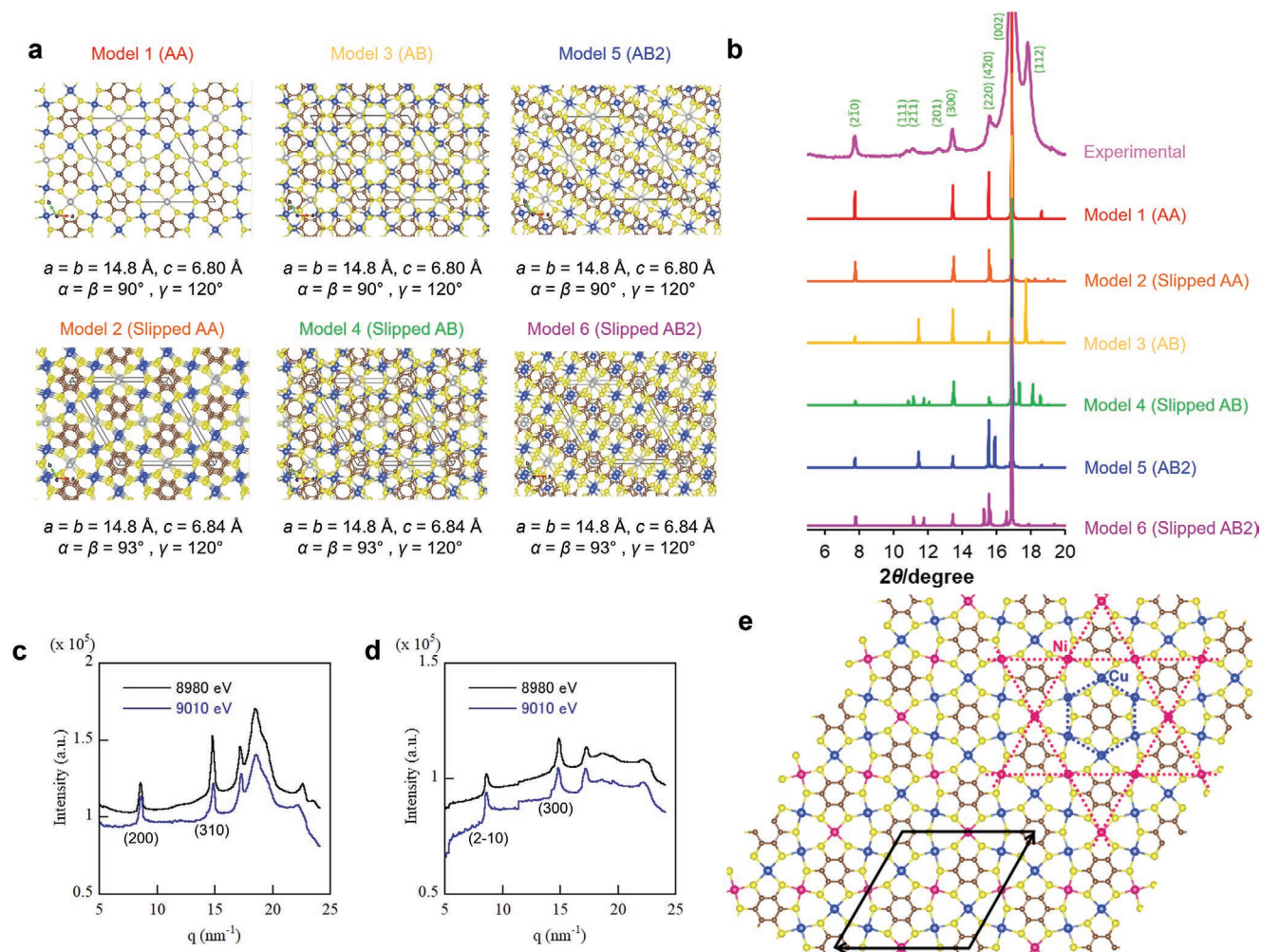
Figure 5. a) Structural models for NiCu₂BHT. Brown, yellow, blue, and silver balls show carbon, sulfur, copper, and nickel atoms, respectively. b) Comparison between experimental and calculated diffraction patterns for the models depicted in (a). c,d) In-plane AGIWAXS pattern of c) Cu₃BHT and d) Ni₀.₄Cu₀.₆/BHT. Intensities are normalized by the first peak. e) Plausible structure for NiCu₂BHT. The unit cell is expressed in a black rhombus.

reaction time to 1 h and using smaller van der Pauw measurement areas (≈500 μm × 500 μm), that were free from visible structural defects as judged according to optical microscopy images. In order to obtain representative values of conductivity for a given sample several different areas on each film were probed (details of the experiment are provided in Experimental Methods). These measurements were done on a probe station on which only the room temperature data could be collected. The electrical conductivity results from two thin film batches are presented in **Figure 6**a. The conductivity values of Ni₃BHT films were generally lower, yet in the range of those in our previous report on Ni₁.₅BHT. A significant increase in conductivity was achieved with increasing copper content, peaking around a Cu fraction of 0.4–0.6, with conductivity values exceeding several hundred S cm⁻¹ and the record values being ≈60% higher than those of pure Cu₃BHT (920 S cm⁻¹ vs 570 S cm⁻¹) for the given batches. The highest conductivity was observed in one synthesis batch of thick films (Figure S15a, Supporting Information), for which a champion conductivity of 1300 S cm⁻¹ was achieved on a Ni₀.₄Cu₀.₆/BHT sample. The excellent charge

transport properties of the heterometallic films are also evident in the near-temperature independence of the conductivity obtained from the same highest performing batch of thick films. To quantify this, we fitted the temperature dependence of the conductivity in a temperature range near room temperature to a thermally activated behavior (Figure S16, Supporting Information). Activation energies of Ni$_x$Cu$_{1-x}$/BHT films with $x = 0.2$ was 0.24 meV while the highly conducting $x = 0.4$ sample shows quasi-metallic behavior with near-temperature independent conductivity and near-zero activation energy (Figure 6b). There is no evidence in these measurements for any increased electronic disorder such as one might have expected in association with a disordered, heterometallic composition and that would have been manifest in stronger temperature activation. If anything, the copper-rich heterometallic films exhibit less electronic disorder than pure Cu₃BHT. This is potentially a manifestation of the bilayer and in-plane ordering among metal sites that is evident from the X-ray measurements. The SEM and AFM images presented in Figure 3e-g and Figures S8 and S9 (Supporting Information) were taken
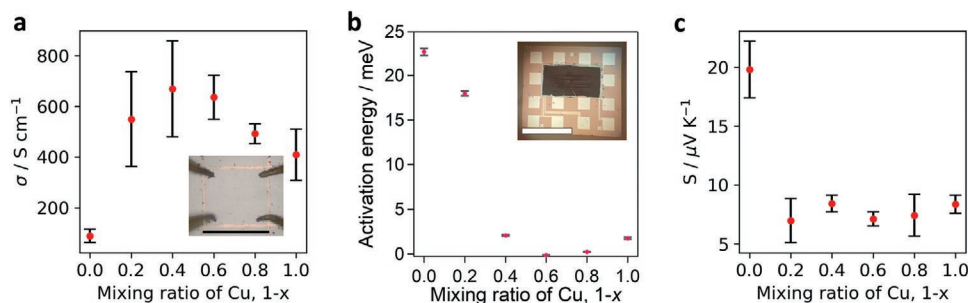
Figure 6. a) Van der Pauw conductivity of Ni_xCu_{1-x}/BHT thin films (reaction time 1 h). The error bars represent standard deviation within the six probing areas for a given composition on the films across two batches. The inset shows the van der Pauw structure used in the low temperature measurements (scale bar ≈ 500 µm). b) Activation energy extracted from the temperature dependent conductivity data of the highest performing batch of Ni_xCu_{1-x}/BHT thick films (reaction time 12 h) in the range of −100 to 0 °C. Error bars denote standard error of the regression from the conductivity trend in Figure S15a in the Supporting Information. The inset shows the van der Pauw device used in the measurement (scale bar = 5 mm). c) Seebeck coefficient of Ni_xCu_{1-x}/BHT thin films (reaction time 1 h). The error bars represent standard deviation within the six measurement areas for a given composition on the films across the two batches.

from the same batch as the films for which conductivity values are presented in Figure S15a in the Supporting Information. For microscopic imaging, the thick film samples were deposited on a silicon wafer, rather than a van der Pauw device. The significant roughness and complex morphology of thick nickel-rich films make it difficult to attribute their low conductivity to potential intrinsic differences in electronic structure as a function of metal composition. In some nickel-rich films, we observed formation of microcracks, indicating significant strain in the films. In such samples, conductivity values were significantly lower than for those shown in Figure 6a. The high conductivity values of copper-rich films are fully consistent with their smooth surface morphology, high crystalline order, and preferential grain orientation (Figure 3).

The Seebeck effect, owing to its intrinsic sensitivity to electronic structure, can provide further insight into electronic properties of materials and is less affected by microstructural defects than the electrical conductivity. Seebeck measurements were performed on the same thin samples, for which conductivity values are presented in Figure 6a. Like in the case of conductivity, the Seebeck coefficient, S, was measured across several different areas on each film (Figure 6c). For all compositions the Seebeck coefficient is positive indicating predominantly hole-type conduction, in contrast to the previous reports on Cu_3BHT,[11a,19] where n-type transport was observed. Given that the studied films have otherwise similar properties, including similar conductivities, this suggests that we may be near a point in the density of states where the conduction changes from n-type to p-type. For the pure copper and heterometallic films we find very similar and low values (<10 µV K^{-1}) of the Seebeck coefficients, only for the pure Ni compositions the Seebeck coefficient is higher (≈20 µV K^{-1}). This can be interpreted as evidence that in the heterometallic films the energy-dependence of the conductivity, which governs the Seebeck coefficient, may not be determined by contributions from metal d-orbitals, but by contributions from carbon p_z orbitals. This appears consistent with recent band structure calculations for Cu_3BHT.[20] It also suggests that doping levels and carrier concentrations are similar across the heterometallic and the pure copper samples. This implies that the conductivity enhancement observed in our heterometallic films compared

to the pure copper ones reflects mainly the increased crystallinity and thus charge carrier mobility rather than changes in the carrier concentration or electronic structure as a function of metal composition. Although the present study is not focussed on optimisation of thermoelectric properties, which would require the tuning of carrier concentrations, it is useful to evaluate power factor values, $S^2\sigma$. These are on the order of 2–5 µW m^{-1} K^{-2} (Figure S17, Supporting Information) similar to those of other MOFs[21]. Notably, the seven-fold increase in the electrical conductivity of the heterometallic films was still outweighed by the higher Seebeck coefficient of the pure Ni_3BHT resulting in a weak dependence of power factor on metal composition.

3. Conclusion

A series of heterometallic, BHT-based, highly conducting, 2D coordination nanosheet films were prepared at a liquid–liquid interface. Serendipitously, a new structural phase was found with intermediate ratios of nickel and copper ions (around Ni/Cu = 1/2). Though full structural characterization of such nanomaterials remains challenging, thanks to their improved crystallinity, an unprecedented bilayer structure and in-plane periodic metal arrangement were revealed, and a plausible structure of $NiCu_2BHT$ was proposed. Electrical conductivities of the films were controlled with the metal ratio by three orders of magnitude, with maximum conductivities of 1300 S cm^{-1} in a copper-rich heterometallic film. Microscopic observation unveiled large, smooth crystalline domains of heterometallic films, which showed lower activation energy and higher conductivities than pure copper films. Considering the preferential formation of a film with improved crystallinity, contrary to our intuition, it might be reasonable to assume that a bilayer structure is the more favorable structural phase for BHT-based coordination nanosheets, rather than the distorted structures of the corresponding homometallic films. Heterometallicity released the structural strain. Our findings open a powerful new pathway to improve the crystallinity and tuning of functional properties of highly conducting coordination nanosheet films for a range of device applications.

**ADVANCED
SCIENCE NEWS**

www.advancedsciencenews.com

**ADVANCED
MATERIALS**

www.advmat.de

4. Experimental Section

Materials: All chemicals were purchased from Tokyo Chemical Industry Co. Ltd., Kanto Chemical Co., Sigma-Aldrich Co. LLC, or Wako Pure Chemical Industries Ltd., unless otherwise stated. They were used without further purification. Benzenehexathiol (BHT) was synthesized according to a previous report.[22]

Instruments: XPS data were obtained using an ULVAC-PHI PHI 5000 VersaProbe spectrometer. Al Kα (15 kV, 25 W) was used as the X-ray source. Spectra were analyzed using MultiPak. The C1s peak at 284.6 eV was used as a standard. Raman spectra were obtained using a HORIBA XploRA PLUS. Ni$_x$Cu$_{1-x}$/BHT film was transferred onto Si/SiO$_2$ substrates and dried in vacuum. A HeNe laser (633 nm, 17 mW) was used for an incident laser after reducing the power to 0.1–1%. Spectra were collected in the range from 2000 to 0 cm^{-1}. The Raman shift was calibrated from the single crystal silicon peak around 520 cm^{-1}. Synchrotron radiation experiments, PXRD measurements were performed at BL44B2 of SPring-8 with a wavelength of 0.8 Å. 2D GIWAXS measurements were performed at BL05XU of SPring-8 with a wavelength of 1.0 Å. Temperature-dependent van der Pauw electrical conductivity of thick films was measured in a commercial Linseis Thin Film Analyzer setup. A measurement current between 10 and 500 µA was employed in the experiments. The room temperature van der Pauw measurements on thin films were done in the probe station using Keithley 2450 SourceMeter following the NIST protocol.[23] A Bruker DektakXT stylus profilometer was used to assess thickness of the thin films in both cases. A small force of 1 mg was used to prevent scratching of the film and the underlying substrate by the profilometer tip. Seebeck measurements were performed on a commercial ZEM-3 (ULVAC-RIKO, Inc.) apparatus. Scanning electron images were taken with an FEI Helios NanoLab 650. A secondary electron detector was used to obtain topography-sensitive contrast in SEM images. An accelerating voltage of 2 kV was used, with a current of less than 6.3 pA. AFM topographic images were obtained on an MFP-3D AFM System (Asylum/Oxford Instruments) in AC (non-contact) mode. Mean square roughness S_q (RMS of height irregularities) calculations were done using Gwyddion SPM data analysis software. ICP analysis was performed using an ICPE-9000 (Shimadzu Corporation). TEM images were recorded at 200 kV of the accelerating voltage using a JEOL JEM-2100F, and EDS analysis was conducted using a JED-2300T. HAADF-STEM images and HAADF-STEM/EDS measurements were collected on a JEOL JEM-ARM200F electron microscope equipped with a thermal field emission gun (Advanced Characterization Nanotechnology Platform, The University of Tokyo) or JEOL JEM-ARM200F NEOARMex electron microscope equipped with a cold field emission gun (JEOL Ltd.). Both electron microscopes were operated at 200 kV.

Synthesis of Heterometallic Films (Ni$_x$Cu$_{1-x}$/BHT): In a glovebox with an oxygen level of less than 2 ppm, 20 mg of BHT-6H were dissolved in dichloromethane (70 mL) to prepare a saturated solution. The undissolved powder was filtered with a syringe filter, and the filtrate was diluted by adding 70 mL of dichloromethane. A 2×10^{-3} M aqueous solution of nickel(II) acetate was prepared by dissolving Ni(OAc)$_2$·4H$_2$O (49.84 mg) in 100 mL of water. Similarly, a copper(II) solution was prepared using 40.02 mg of Cu(OAc)$_2$·H$_2$O. For preparation of heterometallic nanosheets, Ni$_x$Cu$_{1-x}$/BHT, nickel and copper solutions were mixed in a volumetric ratio of x:$(1 - x)$ (2×10^{-3} M in total). 5 mL of the BHT solution was placed in a 20 mL vial. Then, the organic layer was covered with pure water (5 mL) to form a two-phase system. An aqueous solution of metal acetate (2×10^{-3} M, 5 mL) was added slowly to the water layer. The reaction was kept still for 12 h. After that, a black film with a metallic luster formed at the interface. Then, the upper aqueous layer was washed with water (20 mL), and a mixed solvent of water and methanol (1:1, v/v, 20 mL). The bottom layer was washed with dichloromethane (20 mL). During the process, the two layers merged to form a homogeneous phase. All solvent was removed with a pipet, and the film was immersed and stored in methanol. The film was collected on a substrate before measurements.

XAFS Measurement: X-ray absorption spectra (XAS) were acquired in transmission mode using the BL01B1 beamline at SPring-8, employing a double-crystal Si(111) monochromator. Energy values were calibrated by setting the first peak in the Cu foil spectrum equal to 8980.3 eV. EXAFS spectra were analyzed using Athena and Artemis software.

Anomalous Scattering Measurement: Anomalous grazing incidence, wide-angle, X-ray scattering (AGIWAXS) measurements were performed using the BL03XU beamline at SPring-8. Energies of the X-rays were 8980 and 9010 eV, and the sample-to-detector distance was 144 mm. The incident angle of X-rays to the film surface was 0.15 degree. 2D scattering patterns were obtained using a Pilatus3 1M.

Conductivity Measurements: For the temperature dependent measurements of thick films, two sheet resistance measurement sweeps were performed for each measured device to check for repeatability of the measured values, starting from −160 to 20 °C in steps of 10 °C. Films were covered with a spin-coated layer of Cytop, an electrically inactive, fluorinated polymer commonly used as a gate dielectric layer, to prevent electrical contact problems due to film detachment during cryogenic measurements under high-vacuum. The Ohmic nature of the contacts was confirmed prior to every experiment.

Error bars on conductivity ($\delta\sigma$) measurements are propagated from the standard deviation of sheet resistance (δR_s) measurements in the two thermal sweeps, and standard deviation in the mean thickness (δt) values measured at three positions across the films (Figure S18, Supporting Information)

$$\sigma = \frac{1}{\rho} = \frac{1}{R_s \times t} \tag{1}$$

$$\frac{\delta\sigma}{\sigma} = \sqrt{\left(\frac{\delta R_s}{R_s}\right)^2 + \left(\frac{\delta t}{t}\right)^2} \tag{2}$$

where σ denotes conductivity, R_s sheet resistance, and t thickness of the film. The error bar on activation energy represents the standard error in the fitting of the Arrhenius expression for thermally activated conductivity $\sigma = \sigma_0 e^{-E_a/kT}$.

For the room temperature smaller area van der Pauw measurements of thin films, six different areas were probed for a given composition across the two batches of samples. The gold electrical probes provided a clean ohmic contact in all cases. Owing to the smaller area and film uniformity, the uncertainty associated with determination of the film thickness was negligible compared to the standard deviation in the electrical measurements and was not included in the error bars. A representative image of the film with defined van der Pauw area and the corresponding thickness scan are given in Figure S19 in the Supporting Information.

Supporting Information

Supporting Information is available from the Wiley Online Library or from the author.

Acknowledgements

EXAFS experiments were performed using the BL01B1 Beam Line of SPring-8 with the approval of JASRI (Proposal No.2019A1394). The authors acknowledge the Advanced Characterization Nanotechnology Platform (The University of Tokyo) JPMXP09-A-21-UT-0027 for the XPS and HAADF-STEM/EDS measurements. Raman spectroscopy was supported by Y. Soma (Horiba Techno Service Co. Ltd). ICP analysis was supported by Dr. K. Fujimoto and Dr. A. Aimi (Department of Pure and Applied Chemistry, Tokyo University of Science). TEM observations were supported by Prof. Y. Idemoto (Department of Pure and Applied Chemistry, Tokyo University of Science) and Dr. T. Ichihashi (Research Equipment Centre, Tokyo University of Science).

Conflict of Interest

The authors declare no conflict of interest.

Data Availability Statement

The data that support the findings of this study are available from the corresponding author upon reasonable request and in the University of Cambridge repository under https://www.repository.cam.ac.uk/handle/1810/332765.

Keywords

[1] a) C. Li, K. Wang, J. Li, Q. Zhang, *ACS Materials Lett.* **2020**, *2*, 779; b) L. S. Xie, G. Skorupskii, M. Dincă, *Chem. Rev.* **2020**, *120*, 8536; c) H. Maeda, R. Sakamoto, H. Nishihara, *Coord. Chem. Rev.* **2017**, *346*, 139; d) R. Sakamoto, K. Takada, X. Sun, T. Pal, T. Tsukamoto, E. J. H. Phua, A. Rapakousiou, K. Hoshiko, H. Nishihara, *Coord. Chem. Rev.* **2016**, *320–321*, 118; e) M. Wang, R. Dong, X. Feng, *Chem. Soc. Rev.* **2021**, *50*, 2764.

[2] a) X. Huang, H. Yao, Y. Cui, W. Hao, J. Zhu, W. Xu, D. Zhu, *ACS Appl. Mater. Interfaces* **2017**, *9*, 40752; b) E. M. Miner, S. Gul, N. D. Ricke, E. Pastor, J. Yano, V. K. Yachandra, T. V. Voorhis, M. Dincă, *ACS Catal.* **2017**, *7*, 7726; c) H. Jia, Y. Yao, J. Zhao, Y. Gao, Z. Luo, P. Du, *J. Mater. Chem. A* **2018**, *6*, 1188; d) Y. Lian, W. Yang, C. Zhang, H. Sun, Z. Deng, W. Xu, L. Song, Z. Ouyang, Z. Wang, J. Guo, Y. Peng, *Angew. Chem., Int. Ed.* **2020**, *59*, 286; e) H. Zhong, M. Ghorbani-Asl, K. H. Ly, J. Zhang, J. Ge, M. Wang, Z. Liao, D. Makarov, E. Zschech, E. Brunner, I. M. Weidinger, J. Zhang, A. V. Krasheninnikov, S. Kaskel, R. Dong, X. Feng, *Nat. Commun.* **2020**, *11*, 1409.

[3] a) K. Wada, H. Maeda, T. Tsuji, K. Sakaushi, S. Sasaki, H. Nishihara, *Inorg. Chem.* **2020**, *59*, 10604; b) A. Nazir, H. T. T. Le, C.-W. Min, A. Kasbe, J. Kim, C.-S. Jin, C.-J. Park, *Nanoscale* **2020**, *12*, 1629; c) D. Sheberla, J. C. Bachman, J. S. Elias, C.-J. Sun, Y. Shao-Horn, M. Dincă, *Nat. Mater.* **2017**, *16*, 220; d) D. Feng, T. Lei, M. R. Lukatskaya, J. Park, Z. Huang, M. Lee, L. Shaw, S. Chen, A. A. Yakovenko, A. Kulkarni, J. Xiao, K. Fredrickson, J. B. Tok, X. Zou, Y. Cui, Z. Bao, *Nat. Energy* **2018**, *3*, 30; e) J. Park, M. Lee, D. Feng, Z. Huang, A. C. Hinckley, A. Yakovenko, X. Zou, Y. Cui, Z. Bao, *J. Am. Chem. Soc.* **2018**, *140*, 10315.

[4] a) X. Song, X. Wang, Y. Li, C. Zheng, B. Zhang, C. Di, F. Li, C. Jin, W. Mi, L. Chen, W. Hu, *Angew. Chem., Int. Ed.* **2020**, *59*, 1118; b) G. Wu, J. Huang, Y. Zang, J. He, G. Xu, *J. Am. Chem. Soc.* **2017**, *139*, 1360; c) M. K. Smith, K. A. Mirica, *J. Am. Chem. Soc.* **2017**, *139*, 16759.

[5] a) S. Jiang, X. Shi, F. Sun, G. Zhu, *Chem. Asian J.* **2020**, *15*, 2371; b) Y. Liu, R. Sakamoto, C.-L. Ho, H. Nishihara, W.-Y. Wong, *J. Mater. Chem. C* **2019**, *7*, 9159; c) Y. Kuai, W. Li, Y. Dong, W.-Y. Wong, S. Yan, Y. Dai, C. Zhang, *Dalton Trans.* **2019**, *48*, 15121; d) C. Liu, T. Wang, J. Ji, C. Wang, H. Wang, P. Jin, W. Zhou, J. Jiang, *J. Mater. Chem. C* **2019**, *7*, 10240; e) R. Dong, P. Han, H. Arora, M. Ballabio, M. Karakus, Z. Zhang, C. Shekhar, P. Adler, P. S. Petkov, A. Erbe, S. C. B. Mannsfeld, C. Felser, T. Heine, M. Bonn, X. Feng, E. Cánovas, *Nat. Mater.* **2018**, *17*, 1027; f) R. Dong, Z. Zhang, D. C. Tranca, S. Zhou, M. Wang, P. Adler, Z. Liao, F. Liu, Y. Sun, W. Shi, Z. Zhang, E. Zschech, S. C. B. Mannsfeld, C. Felser, X. Feng, *Nat. Commun.* **2018**, *9*, 2637; g) H. Arora, R. Dong, T. Venanzi, J. Zscharschuch, H. Schneider, M. Helm, X. Feng, E. Cánovas, A. Erbe, *Adv. Mater.* **2020**, *32*, 1907063.

[6] T. Kambe, R. Sakamoto, K. Hoshiko, K. Takada, M. Miyachi, J.-H. Ryu, S. Sasaki, J. Kim, K. Nakazato, M. Takata, H. Nishihara, *J. Am. Chem. Soc.* **2013**, *135*, 2462.

[7] T. Kambe, R. Sakamoto, T. Kusamoto, T. Pal, N. Fukui, K. Hoshiko, T. Shimojima, Z. Wang, T. Hirahara, K. Ishizaka, S. Hasegawa, F. Liu, H. Nishihara, *J. Am. Chem. Soc.* **2014**, *136*, 14357.

[8] a) A. J. Clough, J. W. Yoo, M. H. Mecklenburg, S. C. Marinescu, *J. Am. Chem. Soc.* **2015**, *137*, 118; b) A. J. Clough, J. M. Skelton, C. A. Downes, A. A. de la Rosa, J. W. Yoo, A. Walsh, B. C. Melot, S. C. Marinescu, *J. Am. Chem. Soc.* **2017**, *139*, 10863.

[9] T. Pal, T. Kambe, T. Kusamoto, M. L. Foo, R. Matsuoka, R. Sakamoto, H. Nishihara, *ChemPlusChem* **2015**, *80*, 1255.

[10] T. Pal, S. Doi, H. Maeda, K. Wada, C. M. Tan, N. Fukui, R. Sakamoto, S. Tsuneyuki, S. Sasaki, H. Nishihara, *Chem. Sci.* **2019**, *10*, 5218.

[11] a) X. Huang, P. Sheng, Z. Tu, F. Zhang, J. Wang, H. Geng, Y. Zou, C. Di, Y. Yi, Y. Sun, W. Xu, D. Zhu, *Nat. Commun.* **2015**, *6*, 7408; b) X. Huang, S. Zhang, L. Liu, L. Yu, G. Chen, W. Xu, D. Zhu, *Angew. Chem., Int. Ed.* **2018**, *57*, 146.

[12] I.-F. Chen, C.-F. Lu, W.-F. Su, *Langmuir* **2018**, *34*, 15754.

[13] C. M. Tan, M. Horikawa, N. Fukui, H. Maeda, S. Sasaki, K. Tsukagoshi, H. Nishihara, *Chem. Lett.* **2021**, *50*, 576.

[14] a) D. L. Turner, T. P. Vaid, P. W. Stephens, K. H. Stone, A. G. DiPasquale, A. L. Rheingold, *J. Am. Chem. Soc.* **2008**, *130*, 14; b) X. Huang, H. Li, Z. Tu, L. Liu, X. Wu, J. Chen, Y. Liang, Y. Zou, Y. Yi, J. Sun, W. Xu, D. Zhu, *J. Am. Chem. Soc.* **2018**, *140*, 15153.

[15] T. Kusamoto, H. Nishihara, *Coord. Chem. Rev.* **2019**, *380*, 419.

[16] J.-H. Dou, M. Q. Arguilla, Y. Luo, J. Li, W. Zhang, L. Sun, J. L. Mancuso, L. Yang, T. Chen, L. R. Parent, G. Skorupskii, N. J. Libretto, C. Sun, M. C. Yang, P. V. Dip, E. J. Brignole, J. T. Miller, J. Kong, C. H. Hendon, J. Sun, M. Dincă, *Nat. Mater.* **2021**, *20*, 222.

[17] T. Chen, J.-H. Dou, L. Yang, C. Sun, N. J. Libretto, G. Skorupskii, J. T. Miller, M. Dincă, *J. Am. Chem. Soc.* **2020**, *142*, 12367.

[18] H. Banda, J.-H. Dou, T. Chen, N. J. Libretto, M. Chaudhary, G. M. Bernard, J. T. Miller, V. K. Michaelis, M. Dincă, *J. Am. Chem. Soc.* **2021**, *143*, 2285.

[19] R. Tsuchikawa, N. Lotfizadeh, N. Lahiri, Shuwan Liu, M. Lach, C. Slam, J. Louie, V. V. Deshpande, *Phys. Status Solidi A* **2020**, *217*, 2000437.

[20] H. Gao, Z. Wang, X. Ma, X. Zhang, W. Li, M. Zhao, *Phys. Rev. Mater.* **2019**, *3*, 065206.

[21] Y. Fan, Z. Liu, G. Chen, *Small* **2021**, *17*, 2100505.

[22] J. A. Harnisch, R. J. Angelici, *Inorg. Chim. Acta* **2000**, *300–302*, 273.

[23] NANOSCALE DEVICE CHARACTERIZATION DIVISION, Resistivity and Hall Measurements, https://www.nist.gov/pml/nanoscale-device-characterization-division/popular-links/hall-effect/resistivity-and-hall (accessed: December 2021).